Published in final edited form as:
J Am Soc Mass Spectrom. 2009 May ; 20(5): 738–750. doi:10.1016/j.jasms.2009.01.001.

Overtone Mobility Spectrometry (Part 2): Theoretical Considerations of Resolving Power

Stephen J. Valentine, **Sarah T. Stokes**, **Ruwan T. Kurulugama**, **Fabiane M. Nachtigall**, and **David E. Clemmer***
Department of Chemistry, Indiana University, Bloomington, IN 47405

Abstract

The transport of ions through multiple drift regions is modeled in order to develop an equation that is useful for an understanding of the resolving power of an overtone mobility spectrometry (OMS) technique. It is found that resolving power is influenced by a number of experimental variables, including those that define ion mobility spectrometry (IMS) resolving power: drift field (*E*), drift region length (*L*), and buffer gas temperature (*T*). However, unlike IMS, the resolving power of OMS is also influenced by the number of drift regions (*n*), harmonic frequency value (*m*), and the phase number (ϕ) of the applied drift field. The OMS resolving power dependence upon the new OMS variables (*n*, *m*, and ϕ) scales differently than the square root dependence of the *E, L*, and *T* variables in IMS. The results provide insight about optimal instrumental design and operation.

Introduction

When a pulse of ions is injected into a buffer gas, different species separate under the influence of an electric field because of differences in their mobilities through the buffer gas.[1-4] This phenomenon is the basis for a widely used analytical technique for resolving different components of mixtures called ion mobility spectrometry (IMS). The ability to isolate different species can be understood by considering the resolving power ($t_d/\Delta t$), where t_d is the time required for ions to drift through the buffer gas and Δt corresponds to the full width at half maximum (FWHM) of the packet upon exiting the drift region. In the limit of an infinitely narrow injection pulse, the resolving power can be expressed as the ratio of the total drift length (*L*, or t_d) and the spatial width (ΔL, or Δt)) of the ion packet exiting the drift tube.[5] The Einstein relation between the mobility (*K*) and the diffusion coefficient (*D*) (i.e., $D=\sqrt{k_bTK/e}$, where, *e* and k_b correspond to the elementary charge and Boltzmann's constant and *T* is the buffer gas temperature) can be used to estimate ΔL based upon ion displacement leading to an expression for the IMS resolving power (R_{IMS}), Equation 1,[1,5,6]

$$\frac{t}{\Delta t}=\left(\frac{EeL}{16k_bT\ \mathrm{In}\ 2}\right)^{1/2} \quad (1)$$

*To whom correspondence should be addressed. e-mail clemmer@indiana.edu.

Of note is the dependence of resolving power on the square root of the various parameters. This relationship imposes limits on the ultimate instrument performance. For example, doubling L does not double the resolving power; rather, a two-fold increase in L (holding T and E constant) results in only ~40% increase in resolving power.

In the present paper, we report modeling studies of ion transport through multiple drift regions to which the drift fields are applied at varying frequencies, the experimental setup used in overtone mobility spectrometry (OMS). The understanding that is gained from modeling allows us to develop a simple equation that can be used to estimate the OMS resolving power (R_{OMS}). The equation describing the OMS resolving power accounts for a number of geometrical OMS device configurations as well as those parameters used to define R_{IMS}. However, these studies indicate that variation of the parameters which define R_{IMS} (E, L, and T) have only a limited impact on the R_{OMS}. Instead, the factors having the greatest influence on R_{OMS} appear to be the number of phases for the system (i.e., the number of unique drift field application settings as well as the number of drift regions in a complete ion transmission/elimination cycle, see below for complete description), the overall number of ion drift regions, and the drift field setting frequency (overtone number). A surprising result is the unit proportionality relationship between R_{OMS} and the number of drift regions (in effect L) as well as the frequency suggesting the ability to garner much improved instrument performance (with respect to resolution) for proportionate changes when compared with IMS techniques.

It is important to note that the comparisons to R_{IMS} (with respect to L) described here are based on the use of a constant drift field. Equation 1 can be rewritten such that the product of L and E is denoted as the drift voltage (V). Extensive work has shown that increased resolving power can be obtained by optimizing V and the dependence on drift tube length has been described in detail. [7] However, because of the interest in retaining structural information (which can assist ion identification efforts), the comparison has been carried out using low-field conditions which necessitate a square-root dependence on drift length as described herein.

There is currently considerable interest in developing and improving mobility based separation methods. In addition to efforts to improve IMS techniques,[8,9-13] a new method called field asymmetric (FA)IMS has been developed.[8,14-22] Additionally, differential mobility analysis (DMA)[23,24], which has traditionally been used for sizing of particles,[23,25] has been extended for analysis of large molecular systems (such as polymers, proteins and protein complexes).[23,24] The present paper adds to theoretical work associated with understanding these mobility-based techniques.

Methods

Experimental: general description of OMS

It is useful to begin by describing the OMS separation process. For convenience, Table I provides a summary of all variable definitions used in this paper. Since IMS techniques, including descriptions of a range of instruments[26-41] and theoretical treatments[1,6,42-46] are described elsewhere, further discussion of the various techniques is not provided here.

Each OMS instrument contains a specified number (n) of sequential drift regions (d) containing both ion transmission (d_t) and an ion elimination (d_e) regions. In the experimental designs explored so far, the d_e regions constitute a small portion of each d region and are bounded by two electrostatic grids to help maintain drift field uniformity. A dc field is applied across the d_t regions at a defined frequency. This application creates a frequency-dependent repulsive field in some of the d_e regions and this leads to elimination of portions of the continuous ion beam. It is the frequency of, and the order in which, this repulsive field is applied to the d_e regions of the OMS device that serves to transmit ions of specific mobilities. To illustrate the

overall process of OMS measurements we present a description of several instrumental setups and provide examples of experimental data.

Experimental: OMS instrument mode of operation

The mode of operation of an OMS instrument is determined by the number of phases or drift field application settings. This number is denoted by ϕ. Hereafter ϕ represents a positive integer indicating the method of applying drift field pulses to transmit ions of specific mobilities through the OMS device. Figure 1 illustrates a portion of an OMS drift region; eight consecutive d_t regions with accompanying d_e regions are shown. Also shown in Figure 1 are electric field conditions for a two-phase, three-phase, and four-phase system. First consider the operation of a two-phase OMS separation. Here, the drift field settings are modulated between two different settings. As shown in Figure 1, the first field setting (A) consists of multiple regions (each 2*d* in length) the first commencing with the gridded lens immediately preceding $d_t(1)$ and extending to the first gridded lens of the $d_e(2)$ region. At the same time a uniform field is applied to subsequent regions of equal length [e.g., fields across the $d_t(3)$ to $d_e(4)$ regions, the $d_t(5)$ to $d_e(6)$ regions, and the $d_t(7)$ to $d_e(8)$ regions]. This field setting creates repulsive fields in the ion elimination regions $d_e(2)$, $d_e(4)$, $d_e(6)$, and $d_e(8)$. The second field setting (B, in Figure 1) shifts the multiple field regions by one *d* region, and thus the ion elimination regions now become $d_e(1)$, $d_e(3)$, $d_e(5)$, and $d_e(7)$. A complete ion transmission/ elimination cycle shifts from one setting to the other and then back again (e.g., A→B→A for the two-phase system in Figure 1).

To understand the consequences of the field modulation consider the transmission of ions from a continuous ion beam using a two-phase OMS approach. A portion of the continuous ion beam fills the $d_t(1)$ region (Figure 1). Under the first field settings (A in Figure 1), ions are allowed to pass through the $d_e(1)$ region into the $d_t(2)$ region. Then the field is modulated to that of the second setting and the $d_e(2)$ region is set to transmit ions while the $d_e(1)$ region is set to eliminate ions. Thus, ions in the $d_t(2)$ region are transmitted to the $d_t(3)$ region, however, the ions that subsequently filled the $d_t(1)$ region are eliminated in the $d_e(1)$ region. This gives rise to an overall 50% duty cycle for the two-phase OMS system. That is, every other portion of the ion beam filling the $d_t(1)$ region is transmitted down the axis of the OMS device. Transmission of ions in this fashion is only possible if the mobilities of the ions are in resonance with the alternating field settings. That is, ions must have mobilities allowing them to traverse exactly one *d* region in one field application. Ions with mobilities that are off resonance either traversing the *d* region too quickly or too slowly are eventually eliminated in one of the d_e regions. This applied frequency for ions having resonant mobilities is termed the fundamental frequency (f_f).

Having described the field settings for a two-phase system, it is possible to depict the modulation process for a three-phase and a four-phase system. Again the number of distinct field settings is equal to ϕ. Additonally, the number of adjacent *d* regions across which the field is applied is also equal to ϕ and therefore a complete transmission/elimination cycle is equal to ϕ field settings. To understand the impact on ion transmission with increasing ϕ it is instructive to consider operation with a greater number of phases as shown in Figure 1. Here, we consider the four-phase system. As the elimination pulse moves from $d_e(1)$ to $d_e(2)$, ions from the $d_t(1)$ region fill the $d_t(2)$ region. The subsequent field application results in a difference compared with the two-phase operation. Rather than shift back to $d_e(1)$, the elimination pulse moves to $d_e(3)$ and ions from the $d_t(2)$ region move into the $d_t(3)$ region. Additionally, ions from the $d_t(1)$ region move into the $d_t(2)$ region. This proceeds until ions occupy the $d_t(1)$, $d_t(2)$, $d_t(3)$, and $d_t(4)$ regions. At that time, the elimination pulse shifts back to the $d_e(1)$ and ions in the $d_t(1)$ region are eliminated while ions in the other three regions are transmitted throughout the OMS device. Thus a four-phase system has a duty cycle of 75%. Overall, this

discussion leads to a general expression for the duty cycle (neglecting ion diffusion) of an OMS device as a function of phase number (i.e, $1 - \frac{1}{\varphi}$).

Experimentally recorded OMS distributions for different values of φ

OMS distributions can be obtained by recording the ion signal for a specific ion at given field application frequencies. Figure 2 shows the OMS distributions obtained for the $[M + Na]^+$ ion for the oligosaccharide raffinose. The data have been recorded over a range of OMS system phase settings (ϕ = 2 to 6). For each setting for ϕ a dominant peak corresponding to the fundamental frequency is observed. This peak is observed to broaden with increasing ϕ. In addition to the fundamental frequency peak, a number of other peaks are observed for each OMS separation. For example, for the analysis that utilized the two-phase system, peaks are observed at frequencies that are exact multiples of f_f (including $3 \cdot f_f$ and $5 \cdot f_f$). The transmission of ions at "overtone" frequencies is also observed for other values of ϕ. From the experimental data in Figure 2 for raffinose ions (and other ions which show the same behavior) it is clear that the pattern of overtone peaks that are transmitted depends on the magnitude of ϕ. Hereafter the number of the harmonic frequency associated with OMS distribution peaks is denoted by m and is defined as $\phi(h\text{-}1)+1$, where h is a positive integer representing the OMS harmonic index. The harmonic frequency representing the field application frequency setting for ion transmission can thus be expressed as $f_m = m \cdot f_f$. To better understand the process by which ions are transmitted at overtone frequencies, two examples are presented below.

Origin of peaks at overtone frequencies

The origin of overtone peaks can be understood by considering the hypothetical ion beam and transmitted ion distributions that are shown in Figure 3. Here we demonstrate the transmission of ions for the 2nd overtone frequency (m = 3 harmonic) for a two-phase OMS separation. During the first field application, the forward most 1/3 of the ions in the $d_t(1)$ region are transmitted into the $d_t(2)$ region. The elimination field is then shifted to $d_e(1)$ and during this time the middle 1/3 of the ions in the $d_t(1)$ region is eliminated. Upon the next application, the final 1/3 of the ions in the $d_t(1)$ region is transmitted into the $d_t(2)$ region. In this manner, alternating batches of ions are transmitted through the OMS device still yielding a 50% duty cycle (neglecting diffusion). As described in the manuscript published jointly with this work (experimental portion), resolving power increases with increasing m.

From Figure 3 and the discussion given above, we see that transmission of ions at overtone frequencies will also depend on ϕ. For example, for conditions in which the first overtone frequency is applied to a two-phase system, half of the ions in the $d_t(1)$ region [those nearest the $d_e(1)$] are transmitted into the $d_t(2)$ region. However, because m is equal to 2, the second half of the ions in the $d_t(1)$ region are eliminated in the $d_e(1)$ region. During this time, ions in the first half of the $d_t(2)$ region move to the second half of this region. However, elimination subsequently shifts to the $d_e(2)$ region and these ions are eliminated as well. Thus, for the harmonic frequency m = 2 and OMS system phase setting ϕ = 2, ion transmission is not allowed. For the two-phase system, observed harmonic frequencies include m = 1 (fundamental), 3, and 5 (Figure 2). For a four-phase system observed harmonic frequencies include m = 1, 5, 9, and 13 (Figure 2). From these observations and the above rationale, we determine the empirical relation that ions will be transmitted at multiples of the fundamental frequency (i.e., overtones), as mentioned above. Overall, these considerations explain the pattern of peaks that is observed experimentally for different phase values for raffinose (Figure 2).

Because of the relationship between ϕ and m (via h), the focus of the current work is the derivation of an expression for resolving power for those features representing the fundamental and overtone peaks for the different phase systems. These are the major peaks labeled in Figure

2. Here we note that a number of other peaks are observed, most noticeably between the fundamental frequency peak and the $h = 1$ overtone peak for different values of ϕ (particularly for greater values). The origin of these peaks is still under investigation and as such they are not treated here in terms of estimation of resolving power. Rather, investigations focus on the dominant peaks (Figure 2) and their relationship to resolving power.

Ion trajectory simulations

To better understand the separation process of OMS, ion trajectory simulations have been performed. We have used a field array containing 11 *d* regions. The algorithm used to perform the simulations has been written in house and is conceptually similar to those described previously.[47,48] Briefly, the calculations utilize two-dimensional field arrays similar to those generated in SIMION[49] to determine time-dependent ion displacements. The displacement calculation of an ion is the sum of the ion motion contributions from the mobility of the ion (K) as well as its diffusion. The former contribution is field dependent [i.e., the drift velocity is proportional to the product of the mobility and the electric field (KE)] [1], whereas the latter is a randomized contribution in the algorithm (discussed below). Although the algorithm is similar to that described previously,[48] the field arrays of two dimensions are utilized as opposed to three. This change is made because it reduces the time required to model trajectories of thousands of ions. The two dimensions (instead of three) utilized include the ion axis (z-axis) as well as the height (y-axis). Two-dimensional ion trajectory simulations performed in SIMION[49] utilize the same field array dimensions.

The modeling algorithm also allows different OMS phase systems to be examined. For simplicity, trajectory simulations for a two-phase system are described below. The modeling requires two field arrays including one in which the $1+2j$ (j = 0, 1, 2, 3, 4, 5, and 6) d_e regions (see above) contain fields that will transmit ions; the remaining d_e regions contain fields that will cause the elimination of ions. For the second field array, the transmit and eliminate d_e regions are reversed. Initially the algorithm selects one field array and reads in a region (4 field array points) that flanks the two-dimensional position of the ions. A weighted-average field is then calculated for both dimensions based on the distance of the ion to the field values provided at each array point. The displacement due to the ion mobility is then calculated for a user-defined time step (typically ≤ 2μs) using the drift velocity (KE).

Displacement of ions due to diffusion is simulated by

$$\sqrt{\overline{r^2}} = (4D\Delta t)^{1/2} \tag{2}$$

where, $\sqrt{\overline{r^2}}$ is the root mean-square displacement of the ion for time increment Δt and ion diffusion coefficients can be obtained as mentioned above. For ions used in the simulations, K is taken from an experimentally available value (e.g., the mobility of singly-charged bradykinin). To simulate random diffusion in two dimensions, $\sqrt{\overline{r^2}}$ is converted into a polar coordinate vector by randomizing a single angle ($\ominus$). The y- and z-axis vector components are determined from $\sqrt{\overline{r^2}} \cdot sin\ominus$ and $\sqrt{\overline{r^2}} \cdot cos\ominus$, respectively. The diffusion value is then added to the two-dimensional mobility calculation to provide a net ion displacement for each time increment. To perform the trajectory simulation of ions in the two-phase system, a model has been devised where ion origin is referenced with respect to the $d_t(1)$ region immediately preceding the first ion gate [$d_e(1)$]. It is important to note that $d_t(1)$ is equal in size to the other $d_t(n)$ regions (n = 2 to 11). Because the duty cycle of a two-phase system is 50% (neglecting

diffusion, see above), it is only necessary to determine the trajectories of ions as a function of position within this initial $d_t(1)$ region. For the ion trajectory simulations reported here, the $d_t(1)$ region constitutes the first 80 grid units (~5.08 cm) of each field array file. Subsequent d_t regions are of the same length and the conjoining d_e regions are each ~0.32 cm. For the simulations described here, the trajectories for 20 theoretical ions at each location of origin (grid unit) have been simulated. Thus a complete analysis for a specific frequency requires 1600 ion trajectory simulations.

Results and Discussion

Ion trajectory simulations

The trajectory simulations described above have been performed as a function of frequency to provide the peak profiles shown in Figure 4. Each of 10 to 20 incremental frequencies spanning the fundamental frequency as well as the overtones with harmonic frequencies of $m = 3$ and 5 is used. The modeling peak profiles resemble the experimental results on several fronts. First the relative peak heights which are approximately inversely correlated with m are similar to experimentally observed peak heights. Second, the relative resolving powers for the modeled two-phase system [consisting of 11 d regions] are similar to values obtained for peptide ions. That is, resolving powers of ~12, ~28, and ~46 are calculated for the $m = 1$, 3, and 5 frequencies, respectively. This increase in resolving power with increasing overtones is similar to that observed experimentally.

It is instructive to consider which ions in the $d_t(1)$ region are transmitted through the entire mobility device as determined by the ion trajectory simulations. For discussion purposes the $d_t(1)$ region has been divided into 80 initial ion positions and three field application frequencies are considered. Frequencies 1 and 3 (Figure 4) correspond to the left and right, respectively, base of the peak while frequency 2 corresponds to the peak apex (fundamental frequency). For conditions using frequency 1, only ions with initial positions furthest from the $d_e(1)$ region [positions of ~1 to 10 in the $d_t(1)$ region] are effectively transmitted through the OMS device. All other ions are effectively eliminated. For frequency 2, transmission is largely ensured for ions with starting $d_t(1)$ region positions of ~20 to 60 although ion transmission drops off significantly for the far left and right initial ion positions of the $d_t(1)$ region. This is due to the ion diffusion component of the ion trajectory modeling. That is, ions originating in these areas can access preceding or trailing d_e regions for which ion elimination settings are employed. Overall, for frequency 2, the vast majority of the ions in $d_t(1)$ is transmitted through all ion gates and reaches the end of the two-phase OMS device. Frequency 3 produces a transmission profile very similar to frequency 1 with the exception that now the only ions that are transmitted through the instrument are those closest to the $d_e(1)$ region [i.e., those with high initial $d_t(1)$ positions, ~70 to 80]. Examination of such transmission profiles is important because it provides insight necessary for the development of an analytical expression for resolving power (see below). The transmission profile described above is graphically represented as Supplementary Figure 1 in the Supplementary Discussion section.

It is also useful to consider the transmission of ions for a single overtone frequency setting. At the 2nd overtone frequency ($m = 3$), ions are transmitted in the left and right third of the $d_t(1)$ region as shown in Figure 3. Ions in the middle third of the region are eliminated as described above. It is important to note that the smaller transmitted beam portions behave similarly to the larger transmitted portions for the fundamental frequency. That is, it is useful to consider the initial positions of the transmitted ions at the peak base frequencies (frequencies 4 and 6 in Figure 4) as well as the $m = 3$ harmonic (frequency 5 in Figure 4). Using the 80 divisions again for initial starting positions in the $d_t(1)$ region, ions furthest from and closest to the $d_e(1)$ region are transmitted using frequencies 4 and 6, respectively. This occurs for both the front third and the last third of the transmitted $d_t(1)$ region ions. Because of this behavior it is

possible to elucidate a single expression for resolving power that also takes into account overtone frequency transmission. As before, the transmission profile for the $m = 3$ harmonic frequency is shown as a graph (Supplementary Figure 2) in the Supplementary Discussion section.

Developing an analytical expression for estimating resolving power

In order to develop an expression for R_{OMS}, consider results from ion trajectory simulations. Of interest is the peak shape produced by the OMS method. By removing the random diffusion component from the ion displacement calculation in ion trajectory simulations (see above), it is possible to construct a peak shape that depends only on mobility filtering. Peaks produced by measuring ion transmission as a function of frequency (in the f_f region) are *triangular*. As depicted in Supplementary Figure 1, when the frequency increases in the f_f region, the total number of transmitted ions increases in a linear fashion until it reaches a maximum at f_f. From that point, the total number of transmitted ions decreases linearly with increasing frequency until reaching the base of the peak ultimately generating the equilateral triangle peak shape. When the triangular shaped peak is compared to the peak obtained from ion trajectory simulations (i.e. that accounting for diffusion as observed in Figure 4), a slight degree of broadening and apex curvature is observed; the f_f peak shown in Figure 4 is <2% broader than the triangular shape generated in the absence of diffusion. Of interest is the fact that diffusion plays little role in the overall peak width; this is captured in the R_{OMS} expression as described below.

An expression for R_{OMS} can be obtained by considering the particular ions that limit the overall resolving power. For example, at the base of the f_f peak (frequency 1 in Figure 4), only a narrow range of ions [i.e., those furthest from the $d_e(1)$ region] is transmitted through the OMS device. Using this observation it is possible to construct a model from which an equation for resolving power can be derived. The model calls for the determination of the difference from the center of the OMS peak (frequency 2 in Figure 4) to the base of the peak (frequency 1). This difference can then be used to estimate the peak width at half height (Δf_{FWHM}). Because the true peak shape should be very similar to that of an equilateral triangle, this difference would represent ½ of the peak base, or the actual Δf_{FWHM} by definition. From here, it is straightforward to determine the resolving power ($R = f_f / \Delta f_{FWHM}$).

We begin by considering a peak that is associated with ions that are transmitted when the drift field frequency is set to $\sim 1/t_d$ (i.e., the resonant frequency, f_f, for the ions). It is important to note that while ions are optimally transmitted at the resonance frequency, one sees that some ions are also transmitted at slightly lower and higher frequencies, giving rise to the rising and falling edges, respectively, of the peak (shown in Figure 4). The origin of the off-resonance portions of the peak can be understood by considering the initial ion position within the $d_t(1)$ region. Neglecting diffusion, when the ion's mobility matches to the applied frequency, ions at any position in the $d_t(1)$ region will be transmitted to the $d_t(2)$ region. Moreover, at this resonant frequency condition, the ions will occupy the same position in the $d_t(2)$ region after one drift field application setting. An ion starting at position 1 (See Supplementary Figure 1) in the $d_t(1)$ region will arrive at position 1 of $d_t(2)$. To reach the last elimination region, $d_e(n)$, will require n field application settings (n/2 transmission and elimination cycles for a two-phase system).

Now consider conditions where the applied frequency is lower than the ion's resonant fundamental frequency (frequency 1 in Figure 4). With each pulse all ions arrive at a position that is slightly more displaced within the next d region (e.g., for the ion described above, position numbers of 10 and 20 in the $d_t(2)$ and $d_t(3)$ regions, respectively). An extreme case would be those ions having the greatest mismatch in mobility frequency and gating frequency. For the ion described above (i.e., starting at position 1) to be transmitted, it would need to reach

the last d_e region just before the drift field was switched from elimination to transmission (i.e., requiring one fewer or *n-1* field application settings). This represents the worst case scenario; if the frequency/mobility mismatch were any greater (lower frequency field application), then the switch from elimination to transmission would occur at a longer time and the ion would have been eliminated at $d_e(n)$. In the limit of an infinitely small d_e region, it can be argued that for the fundamental frequency setting, the ion would have experienced *n* field application settings while for the frequency 1 setting (Figure 4) the ion would have experienced *n-1* field application settings in the same time (t_{total} = time required to reach the n^{th} gate).

With an understanding that the time duration of a single field application setting (P_w) is equal to t_{total} divided by the total number of settings, we can obtain expressions for the field application time associated with the fundamental frequency (f_2 in Figure 4), as well as that associated with the base of the peak frequency (f_1 in Figure 4). Equations for the former and latter are shown in Equations 3 and 4, respectively,

$$P_{w2}=\frac{^{t}total}{n} \tag{3}$$

$$P_{w1}=\frac{^{t}total}{n-1} \tag{4}$$

These relationships can be used to relate the frequencies of f_1 and f_2 (see supplementary information) leading to Equation 5,

$$f_1=\frac{(n-1)\,f_2}{n} \tag{5}$$

Understanding that OMS peaks are triangular in nature and using Equation 5, it is possible to obtain the simplified expression for ROMS shown in Equation 6 (see supplementary information for equation derivation information details).

$$R_{OMS}=n \tag{6}$$

Remarkably, the resolving power of the OMS technique for the fundamental peak depends only on the number of drift region segments. Although this is somewhat intuitive, it stands as an important result because it defines one important difference between OMS, where R_{OMS} scales directly with L (here L is equal to n multiplied by the length of the d region), and IMS, where R_{IMS} scales with $\sqrt{L}$.

Inclusion of overtone frequency terms

With an expression for the resolving power of the fundamental frequency, it is useful to include the effects of OMS system phase and harmonic frequency. Consider the case of the four-phase OMS device. Here, four ion gating regions are triggered sequentially to complete one transmission/elimination cycle. As described above, ions occupying the space of three *d* regions are transmitted through the OMS device for every space equivalent to one *d* region that leads to ion elimination (i.e., a duty cycle of 75%). Because the total ion transmission range is three

times larger than the comparable two-phase system (i.e., one with d regions of identical length), the difference in number of pulses experienced by ions using field application frequencies f_1 and f_2 (Figure 4) is three. And thus the R_{OMS} scales as $\frac{n}{3}$ (see Supplementary Information for more details on this dependency). Although the signal level increases with increasing phase, the resolving power is lower by a factor of $(\phi\text{-}1)^{-1}$ for a given value of n.

The opposite effect is observed with an increase in overtone. Consider the two-phase system operating at the $m = 3$ harmonic frequency (2^{nd} overtone). Because the overall frequency is three times greater than f_1, the total number of field applications experienced by an ion at the $m = 3$ harmonic frequency transmission region is three times the number of d regions or $3n$. Ions at the base of the OMS peak profile (e.g., frequency 4 in Figure 4) will experience one fewer field application setting ($3n\text{-}1$) over the same time period. Thus, using the same derivation as that for Equation 6 (see supplementary information), R_{OMS} is observed to scale directly with the product of m and n.

Consideration of the sizes of transmission and elimination regions

Until this point, the d_e regions were treated as infinitely small. It is interesting to consider the consequences of different lengths of d_t and d_e regions (denoted l_t and l_e, respectively). Consider the two-phase system. As mentioned above the difference in number of pulses experienced for ions at a field application frequency of f_1 versus a field application frequency of f_2 is $n\text{-}1$ and n, repsectively. However, in order to be transmitted, over the same time period these ions are required to arrive just before (for the f_1 field application settings in Figure 4) and just after (for the f_2 field application settings in Figure 4) the last d_e region. In these scenarios, the last d_e region would be switching from eliminate to transmit and transmit to eliminate, respectively. These situations are only possible in the limit of an infinitely small l_e. Due to the fact that l_e is greater than zero, the f_1:f_2 ratio of n-1:n (Equation 5) should be revised. Because ions do not traverse the entire length of the last d region for the f_1 field settings (compared to the f_2 settings), the difference in the number of field application settings is less than one. That is, the n-1 term can be corrected by a factor related to the change in distance traversed by the ions. The new term becomes $n - 1\left[\frac{l_t}{l_t+l_e}\right]$. As noted above, this term is used to relate f_1 and f_2.

With an understanding of the influence of n, ϕ, m, as well as l_t and l_e on the relationship between f_1 and f_2, it is possible to obtain the following expression for R_{OMS}:

$$R_{OMS} = \frac{mn}{\varphi - 1 - \frac{l_e}{l_t+l_e}} \tag{7}$$

This expression reveals several important factors affecting the overall resolving power. First, as observed above, R_{OMS} increases linearly with increasing n. Similarly, R_{OMS} increases linearly with m; that is, higher harmonic frequencies result in increased resolving power. However, the equation demonstrates that an increase in the number of phases of the system actually decreases the R_{OMS}. The final factor affecting R_{OMS} is the ratio of l_e to l_t. As this ratio increases, R_{OMS} increases.

Inclusion of diffusion

It is important to note that Equation 7 does not truly represent a worst-case scenario for the greatest mismatch in f_1 and f_2 since this expression does not include ion diffusion. The situation that would lead to the greatest influence on resolving power is if the ion diffusion is

unidirectional. That is, net diffusion in the direction opposite the direction of mobility motion results in the greatest mismatch between f_1 and f_2. If an average velocity of diffusion (v_{dif}) is subtracted from the drift velocity (KE) used to calculate R_{OMS} (see the supplementary information), f_1 is decreased resulting in a wider base of the OMS peak. By introducing a diffusion component into the calculation it is possible to express R_{OMS} in terms of R_{IMS}. The final R_{OMS} equation accounting for all experimental parameters becomes,

$$R_{OMS} = \frac{1}{1 - \left[1 - \frac{C_2}{R_{IMS}}\right]\left[\frac{mn - \left[\varphi - 1 - \frac{l_e}{l_t + l_e}\right]}{mn}\right]} \quad (8)$$

Here C_2 corresponds to a constant allowing the conversion to R_{IMS} ($C_2 \approx 0.74$).

Equation 8 provides insight about limits associated with diffusion. That is, in the limit of high R_{IMS} (less diffusion), the denominator approaches a minimum value leading to a maximum R_{OMS}.

Evaluation of the OMS resolving power equation: dependence on number of gating regions and applied frequency

We begin the evaluation of the expression for OMS resolving power by considering several experimental results. Figure 5 shows the experimental peak widths for the $[M + Na]^+$ ion of the trisaccharide melezitose for varying numbers (n) of d regions. The data have been acquired by applying the fundamental frequency for a four-phase OMS device. The results show a substantial decrease in peak width with increasing n. At $n = 11$, the measured FWHM is ~1600 Hz, whereas a value of ~345 Hz is obtained at $n = 43$. This large dependence on n is intriguing because it suggests that OMS resolving power is not defined by a square root dependence on L as is the case for IMS experiments. To evaluate the efficacy of the equation for predicting OMS resolving power as a function of n, calculated values have been compared to the experimental results obtained for the four-phase OMS system (Figure 5). The equation predicts a linear increase in R_{OMS} from 3.6 to 13.0 at n-values of 11 and 43, respectively. A linear fit to the calculated values provides a line with a slope of 0.293 and an intercept of 0.471 (R^2 = 0.999). The comparison shows that the trend of increasing resolving power with an increase in n is observed for both the experimental data and the calculated values. On average, the equation predicts a resolving power that is ~37% higher than what is obtained experimentally. Calculated resolving power and experimentally determined values are shown as Supplementary Figure 3 in the Supplementary Information section.

The ability of the equation to predict resolving power as a function of the applied overtone frequency has also been investigated. The comparison has been evaluated using experimental data for three different systems ($\phi = 2$, 3, and 4). Additionally, the transmitted overtone peaks (for which h=2 to 3) of each system have been compared. The results of the comparison are shown in Figure 6. In general, the agreement is as observed before with the equation providing a resolving power that is ~21% higher on average than experimental results for the fundamental frequency and the overtone frequencies (corresponding to h=2 to 3). For all systems, the trend of increasing resolving power with increasing applied frequency is observed. The equation is also able to mimic the observation of increased resolving power with decreasing OMS phase number. In addition to this, the equation, as with the experimental data, shows an increased rate of resolving power improvement (from the fundamental frequency to the overtone frequency corresponding to h=2) as a function of decreasing phase number. Finally, it should be noted that for the calculated resolving power, the rate of increase is greatest from the fundamental frequency to the overtone frequency corresponding to h=2. At that point, going

from the h = 2 to 3 overtone frequencies allowing ion transmission, the rate of increase is not as high. This occurs for each OMS phase system. Intuitively, this occurs because of the decrease in size of the transmitted ion beam portion (Figure 3). While this portion of the beam is decreasing with increasing overtone frequency, the overall ion transit time is not. Thus diffusion becomes more significant for this shorter transmitted beam. Because, diffusion is overestimated in our resolving power equation (as the maximum expected value), the theoretical values drop below the experimental values.

Evaluation of the resolving power equation: dependence on diffusion

The OMS resolving power equation can be used to begin to evaluate factors involving ion diffusion and their influence on the overall attainable resolving power. The resolving power has been evaluated as a function of two parameters from Equation 1 that affect the degree of ion diffusion; these are E and T. Here we note that from our treatment of L [$n\cdot(l_t + l_e)$], we observed a negligible effect from diffusion over the experimental range of L (Supplementary Figure 3). For the determination of the effect of E and T, a comparison of the m = 1, 3, and 5 harmonic frequencies for a two-phase system has been carried out. The overall change for both parameters is relatively small across reasonable instrumentation operating ranges and is most pronounced for the m = 5 frequency. For example, from E = 7 V·cm^{-1} to E = 25 V·cm^{-1} only an ~39% improvement in resolving power is observed; similarly, the range of T = 200 to 400 K exhibits only an ~29% improvement in resolving power (going from high to low temperatures). This analysis serves as a nice double check of the resolving power equation. That is, the boundaries for improved resolving power are the same as those expected from IMS measurements. A difference is the limited effect of ion diffusion on overall resolving power for OMS experiments (under current operating conditions). The effects of E and T can be observed in Supplementary Figure 4 in the Supplementary Information section.

Although, diffusion does not appear to affect the resolving power significantly, it is useful to consider a possible explanation for the observation of a larger change at higher overtone numbers. As mentioned above, the transmitted ion beam portions are much smaller for the higher overtones (Figure 3). The contribution of diffusion becomes more significant for these shorter ion beam portions (note the overall transit time is not changed). That is, the distance travelled due to diffusion (counter to the mobility of the ion for the OMS resolving power equation) is a larger percentage of the overall transmission region size.

Another factor that influences the degree of peak broadening due to diffusion is the ratio of the transmit and elimination (l_t and l_e) region length. To assess the effect of these lengths on computed resolving power, each is held constant while the other is varied. Four preliminary studies, summarized in Table I, were carried out. The first involves the changing of the l_e region while maintaining a constant value for l_t. In general, the resolving power increases for increasing l_t. This result again suggests that peak broadening due to diffusion is worse for smaller ion beam portions as we have discussed above. The next study involves the maintaining of the combined length ($l_e + l_t$), while changing the ratio of the two regions. That is, in one instance one region is much greater than the other and then the distances are reversed. Increasing the length of the l_e region has a much greater impact in improving resolving power. Upon observation of the equation this becomes clearer. As l_e increases, the term containing n becomes larger than $\frac{n-1}{n}$. That is the difference in pulse widths at the base and apex of the peak in the OMS spectrum (Figure 4) becomes smaller leading to an increase in resolving power. The fourth study involves computing R_{OMS} for equi-distant l_t and l_e regions which does not significantly impact R_{OMS} except when compared to instances where l_e is significantly smaller. The final study involves changing the l_e region while maintaining the l_t region. Here only a modest increase in resolving power is achieved. Based on the above studies, it appears that by increasing l_e substantially, a significant improvement in resolving power can be

obtained. However, in considering the origin of the ions that limit resolving power, the only method by which ions of the same mobility arrive at drastically different positions in the OMS device over the same time period is due to diffusion. Therefore, there is a limit to the size of the l_e region after which ion transmission would be blocked. Additionally, a larger l_e leads to a decrease in experimental duty cycle.

The computed values in Table 2 show that the resolving power equation can be used to rapidly test the separation efficiency of specific instrumental configurations. An understanding of the trends for each of the variables suggests the direction in which one should pursue higher resolving power. Another interesting feature of the table is that a relatively high resolving power (~85) can be obtained with a fairly small device.

The use of OMS for structural analysis

Until now the discussion has focused on the ability to estimate R_{OMS} for a given OMS experimental setup. Briefly the discussion has touched upon the application of OMS as a mobility selection device. As a final thought, an application of ion structure analysis is discussed. As mentioned above, the measurement of K by IMS can be used to make inferences about the shapes of specific ions. This is accomplished by using measured values of K to determine a collision cross section from,[1]

$$\Omega=\frac{(18\pi)^{1/2}}{16}\frac{ze}{(k_bT)^{1/2}}\left[\frac{1}{m_I}+\frac{1}{m_B}\right]^{1/2}\frac{t_DE}{L}\frac{760}{P}\frac{T}{273.2}\frac{1}{N} \quad (9)$$

where P and N correspond to the buffer gas pressure and the neutral number density under STP conditions, respectively. The variable m_I and m_B correspond to the mass of the ion and the mass of the buffer gas, respectively. The variables E, L, P, and t_D can be measured accurately providing high accuracy cross section determinations.

To obtain a collision cross section from an OMS measurement, the distance the ion travels in a specified amount of time must be determined. From an OMS distribution this translates into ion displacement over the time equal to the inverse of the peak apex frequency. For the fundamental frequency, recalling that ion displacement corresponds to one d region, the calculation is relatively straightforward. For conditions that employ overtone frequencies (m>1), recall that ion displacement is equal to a fraction of the d region (or d/m, see Figure 3). Additionally, because m can be expressed in terms of ϕ and h [i.e., $m=\phi(h\text{-}1)+1$], it becomes possible to rewrite Equation 25 for OMS measurements as,

$$\Omega=\frac{(18\pi)^{1/2}}{16}\frac{ze}{(k_bT)^{1/2}}\left[\frac{1}{m_I}+\frac{1}{m_B}\right]^{1/2}\frac{E\left[\varphi(h-1)+1\right]}{f(l_t+l_e)}\frac{760}{P}\frac{T}{273.2}\frac{1}{N} \quad (10)$$

One concern about the measurement of cross sections in a device that uses electrodynamic fields is the effect of the voltage slewing rate on the overall measurement. Experiments have shown that ~20 ns are required to achieve stable fields after switching. From a number of experiments, for a variety of ions (different charge states of ubiquitin, peptides, and carbohydrates), the cross sections obtained from OMS measurements differ from those obtained by IMS techniques by 2 to 4% on average. Noting that this difference is larger than the errors obtained for different IMS instruments (typically < 2%), it is possible that a portion may indeed result from field inhomogeneity. It may also result from slight errors in the

determination of drift region segment length. The propagation of such an error would be more problematic than a small error in the overall length of a drift tube for an IMS instrument.

The ability to determine accurate collision cross sections may serve a number of applications. One example may include aiding in the identification of mixture components. That is, with significant enhancements to component resolution, cross sections determined for features in OMS distributions can be compared against trial structures.[43,50-62] Such an approach could be used to select specific structures for further analysis.

Summary

Simulations involving the transport of ions through multiple drift regions have been compared with experimental data in order to develop a better understanding of the origin of resolving power in OMS. The results lead to an expression for resolving power that includes experimental variables associated with ion diffusion (E, L, and T) as well as variables related to OMS instrument operation (ϕ, n, f, d_t, and d_e). The impact of the various parameters on resolving power was described. A surprising result of the current study is the unit proportionality observed for the number of drift regions and the overall frequency. This observation is distinguished from that for conditions affecting the resolving power of traditional IMS techniques in that, for R_{OMS}, greater improvements in resolving power are provided per percent change in parameters affecting resolving power. Overall, this understanding suggests that it should be possible to build instruments with relatively high resolving power that are capable of transmitting ions with well defined mobilities.

Supplementary Material

Refer to Web version on PubMed Central for supplementary material.

Acknowledgments

The development of new instrumentation is supported in part by a grants from the National Institutes of Health (AG-024547-01 and P41-RR018942), and the METACyte initiative funded by a grant from the Lilly Endowment. The authors are grateful for numerous stimulating discussions with their colleagues, Liang-shi Li, Caroline C. Jarrold, and Gary M. Hieftje about overtones and instrumentation in general. We also thank John Poehlman and Andrew Alexander for technical support.

References

1. Mason, EA.; McDaniel, EW. Transport Properties of Ions in Gases. Wiley; New York: 1988.
2. For a review of IMS techniques see (and references therein): St Louis RH, Hill HH. Ion mobility spectrometry in analytical chemistry. Crit Rev Anal Chem 1990;21:321.
3. For a review of IMS techniques see (and references therein): Clemmer DE, Jarrold MF. Ion mobility measurements and their applications to clusters and biomolecules. J Mass Spectrom 1997;32:577–592.592
4. For a review of IMS techniques see (and references therein): Hoaglund Hyzer CS, Counterman AE, Clemer DE. Anhydrous protein ions. Chem Rev 1999;99:3037–3079.3079 [PubMed: 11749510]
5. Kemper PR, Bowers MT. Electronic-state chromatography –application to 1st-row transition-metal ions. J Phys Chem 1991;95:5134–5146.
6. Revercomb HE, Mason EA. Theory of plasma chromatography gaseous electrophoresis – review. Anal Chem 1975;47:970–983.
7. Siems WF, Wu C, Tarver EE, Hill HH, Larsen PR, McMinn DG. Measuring the resolving power of ion mobility spectrometers. Anal Chem 1994;66:4195.

8. Tang K, Li F, Shvartburg AA, Stritmatter EF, Smith RD. Two-dimensional gas-phase separations coupled to mass spectrometry for analysis of complex mixtures. Anal Chem 2005;77:6381–6388. [PubMed: 16194103]
9. Dougard P, Hudgins RR, Clemmer DE, Jarrold MF. High-resolution ion mobility measurements. Rev Sci Instrum 1997;119:2240.
10. Wu C, Siems WF, Asbury GR, Hill HH. Electrospray ionization high-resolution ion mobility spectrometry-mass spectrometry. Anal Chem 1998;70:4929–4938.
11. Srebalus CA, Li J, Marshall WS, Clemmer DE. Gas-phase separations of electrosprayed libraries. Anal Chem 1999;71:3918–3927. [PubMed: 10500479]
12. Tang K, Shvartsburg AA, Lee HN, Prior DC, Buschbach MA, Li F, Tolmachev A, Anderson GA, Smith RD. High-sensitivity ion mobility spectrometry/mass spectrometry using electrodynamic ion funnel interfaces. Anal Chem 2005;77:3330–3339. [PubMed: 15889926]
13. Merenbloom SI, Koeniger SL, Bohrer BC, Valentine SJ, Clemmer DE. Improving the efficiency of IMS-IMS by a combing technique. Anal Chem 2008;80(6):1918–1927. [PubMed: 18290667]
14. Shvartsburg AA, Smith RD. Scaling the resolving power and sensitivity for planar FAIMS and mobility-based discrimination in flow- and field-driven analyzers. J Am Soc Mass Spectrom 2007;18:1672–1681. [PubMed: 17723907]
15. Carnahan B, Day S, Kouznetsov V, Matyjaszczuk M, Tarassov A. Field ion spectrometry – a new analytical technology for trace gas analysis. Proceedings of the International Conference on Advance in Instrumentation and Control ISA 1996:87–95.
16. Purves RW, Guevremont R, Day S, Pipich CW, Matyjaszcayk MS. Mass spectrometric characterization of a high-field asymmetric waveform ion mobility spectrometer. Rev Sci Instrum 1998;69:4094.
17. Purves RW, Guevremont R. Electrospray ionization high-field asymemetric waveform ion mobility spectrometry-mass spectrometry. Anal Chem 1999;71:2346–2357.
18. Eiceman GA, Tadjikov B, Krylov E, Nazarov EG, Miller RA, Westbrook J, Funk P. Miniature radio-frequency mobility analyzer as a gas chromatographic detector for oxygen-containing volatile organic compounds, pheromones and other insect attractants. J Chromatogr A 2001;917:205–217. [PubMed: 11403471]
19. Venne K, Bonneil E, Eng K, Thibault P. Improvement in peptide detection for proteomics analyses using nanoLC-MS and high-field asymmetry wafeform ion mobility mass spectrometry. Anal Chem 2005;77:2176–2186. [PubMed: 15801752]
20. Barnett DA, Purves RW, Ells B, Guevremont R. Separation of o-, m- and p-phthalic acids by high-field asymmetric waveform ion mobility spectrometry (FAIMS) using mixed carrier gases. J Mass Spectrom 2000;35(8):976–980. [PubMed: 10972997]
21. Guevremont R, Purves R. Comparison of experimental and calculated peak shapes for three cylindrical geometry FAIMS prototypes of differing electrode diameters. J Am Soc Mass Spectrom 2005;16(3):349–362. [PubMed: 15734328]
22. Guevremont R, Thekkadath G, Hilton CK. Compensation voltage (CV) peak shapes using a domed FAIMS with the inner electrod translated to various longitudinal positions. J Am Soc Mass Spectrom 2005;16(6):948–956. [PubMed: 15907709]
23. Rossell-Llompart J, Loscertales IG, Bingham D, de la Mora JF. Sizing nanoparticles and ions wiht a short differential mobility analyzer. J Aerosol Sci 1996;27(5):695–719.
24. Labowsky M, de la Mora JF. Novel ion mobility analyzers and filters. J Aerosol Sci 2006;37(3):340–362.
25. For a recent review regarding the history of DMA for analysis of particles see (and references therein): McMurry PH. A review of atmospheric aerosol measurements. Atmospheric Environment 2000;34:1959–1999.1999
26. Wittmer D, Luckenbill BK, Hill HH, Chen YH. Electrospray-ionization ion mobility spectrometry. Anal Chem 1994;66:2348–55.
27. Clemmer DE, Hudgins RR, Jarrold MF. Naked protein conformations – cytochrome-c in the gas-phase. J Am Chem Soc 1995;117:10141–42.

28. von Helden G, Wyttenbach T, Bowers MT. Conformation of macromolecules in the gas-phase –use of matrix-assisted laser-desorption methods in ion chromatography. Science 1995;267:1483–85. [PubMed: 17743549]
29. von Helden G, Wyttenbach T, Bowers MT. Inclusion of a MALDI ion-source in the ion chromatography technique –conformational information on polymer and biomolecular ions. Int J Mass Spectrom Ion Process 1995;146:349–364.
30. Chen YH, Siems WF, Hill HH Jr. Fourier transform electrospray ion mobility spectrometry. Anal Chim Acta 1996;334(12):75–84.
31. Gillig KJ, Ruotolo B, Stone EG, Russell DH, Fuhrer K, Gonin M, Schultz AJ. Coupling high-pressure MALDI with ion mobility/orthogonal time-of-flight mass spectrometry. Anal Chem 2000;72:3965–3971. [PubMed: 10994952]
32. Hoaglund CS, Valentine SJ, Sporleder CR, Reilly JP, Clemmer DE. Three-dimesional ion mobility/TOFMS analysis of electrosprayed biomolecules. Anal Chem 1998;70:2236–2242. [PubMed: 9624897]
33. Hoaglund-Hyzer CS, Li J, Clemmer DE. Mobility labeling for parallel CID of ion mixtures. Anal Chem 2000;72:2737–2740. [PubMed: 10905301]
34. Bluhm BK, Gillig KJ, Russell DH. Development of a fourier-transform ion cyclotron resonance mass spectrometer-ion mobility spectrometer. Rev Sci Instrum 2000;71(11):4078–4086.
35. Hoaglund-Hyzer CS, Clemmer DE. Ion trap/ion mobility/quadrupole/time-of-flight mass spectrometry for peptide mixture analysis. Anal Chem 2001;73:177–184. [PubMed: 11199963]
36. Counterman AE, Clemmer DE. Large anhydrous polyalanine ions: evidence for extended helices and onset of a more compact structure. J Am Chem Soc 2001;123:1490–1498. [PubMed: 11456724]
37. Valentine SJ, Kulchania M, Barnes CAS, Clemmer DE. Multidimensional separations of complex peptide mixtures: a combined high-performance liquid chromatography/ion mobility/time-of-flight mass spectrometry approach. Int J Mass Spectrom 2001;212:97–109.
38. Myung S, Badman E, Lee YJ, Clemmer DE. Structural transitions of electrosprayed ubiquitin ions stored in an ion trap over ~10 ms to 30 s. J Phys Chem A 2002;106:9976–9982.
39. Tang K, Shvartsburg AA, Lee HN, Prior DC, Buschbach MA, Li FM, Tolmachev AV, Anderson GA, Smith RD. High-sensitivity ion mobility spectrometry/mass spectrometry using electrodynamic ion funnel interfaces. Anal Chem 2005;77:3330–3339. [PubMed: 15889926]
40. Clowers BH, Siems WF, Hill HH, Massick SM. Hadamard transform ion mobility spectrometry. Anal Chem 2006;78(1):44–51. [PubMed: 16383309]
41. Sun WJ, May JC, Russell DH. A novel surface-induced dissociation instrument for ion mobility-time-of-flight mass spectrometry. Int J Mass Spectrom 2007;259(13):79–86.
42. Mack E. Average cross-sectional areas of molecules by gaseous diffusion methods. J Am Chem Soc 1925;47:2468–2482.
43. Shvartsburg AA, Jarrold MF. An exact hard-spheres scattering model for the mobilities of polyatomic ions. Chem Phys Lett 1996;261:86–91.
44. Mesleh MF, Hunter JM, Shvartsburg AA, Schatz GC, Jarrold MF. Structural information from ion mobility measurements: effects of the long-range potential. J Phys Chem 1996;100:16082–16086.
45. Wyttenbach T, von Helden G, Batka JJ, Carlat D, Bowers MT. Effect of the long-range potential on ion mobility measurements. J Am Soc Mass Spectrom 1997;8:275–282.
46. Shvartsburg AA, Hudgins RR, Dugourd P, Jarrold MF. Structural information from ion mobility measurements: applications to semiconductor clusters. Chem Soc Rev 2001;30:26–35.
47. Julian RR, Mabbett SR, Jarrold MF. Ion funnels for the masses: experiments and simulations with a simplified ion funnel. J Am Soc Mass Spectrom 2005;16(10):1708–1712. [PubMed: 16095911]
48. Koeniger SL, Merenbloom SI, Valentine SJ, Jarrold MF, Udseth H, Smith RD, Clemmer DE. An IMS-IMS analogue of MS-MS. Anal Chem 2006;68:4161–4174. [PubMed: 16771547]
49. Dahl, DA. SIMION (Version 7.0). Idaho National Engineering Laboratory; Idaho Falls, ID:
50. Mack E. Average cross-sectional areas of molecules by gaseous diffusion methods. J Am Chem Soc 1925;47:2468–2482.
51. von Helden G, Hsu M–T, Kemper PR, Bowers MT. Structures of carbon cluster ions from 3 to 60 atoms –linears to rings to fullerenes. J Chem Phys 1991;95(5):3835–3837.

52. Jarrold MF, Constant VA. Silicon cluster ions –evidence for a structural transition. Phys Rev Lett 1991;67(21):2994–2997. [PubMed: 10044611]

53. von Helden G, Hsu M–T, Gotts N, Bowers MT. Carbon cluster cations with up to 84 atoms –structures, formation mechanism, and reactivity. J Phys Chem 1993;97:8182–8192.

54. Shelimov KB, Hunter JM, Jarrold MF. Small carbon rings –dissociation, isomerization, and a simple-model based on strain. Int J Mass Spectrom Ion Phys 1994;138:17–31.

55. Clemmer DE, Hudgins RR, Jarrold MF. Ion mobility measurements and their applications to clusters and biomolecules. J Am Chem Soc 1995;117:10141–42.

56. Mesleh MF, Hunter JM, Shvartsburg AA, Schatz GC, Jarrold MF. Structural information from ion-mobility measurements: effects of the long-range potential. J Phys Chem 1996;100:16082–16086.

57. Wyttenbach T, von Helden G, Batka JJ, Carlat D, Bowers MT. Effect of the long-range potential on ion mobility measurements. J Am Chem Soc 1997;8:275–282.

58. Shvartsburg AA, Hudgins RR, Dugourd P, Jarrold MF. Structural information from ion mobility measurements: applications to semiconductor clusters. Chem Soc Rev 2001;30:26–35.

59. Valentine SJ, Anderson JG, Ellington AD, Clemmer DE. Disulfide-intact and –reduced lysozyme in the gas phase: conformations and pathways of folding and unfolding. J Phys Chem B 1997;101:3891–3900.

60. Hudgins RR, Ratner MA, Jarrold MF. Design of helices that are stable in vacuo. J Am Chem Soc 1998;120:12974–75.

61. Counterman AE, Clemmer DE. Large anhydrous polyalanine ions: evidence for extended helices and onset of a more compact state. J Am Chem Soc 2001;123:1490–1498. [PubMed: 11456724]

62. Myung S, Badman E, Lee YJ, Clemmer DE. Structural transitions of electrosprayed ubiquitin ions stored in an ion trap over ~10 ms to 30 s. J Phys Chem A 2002;106:9976–9982.

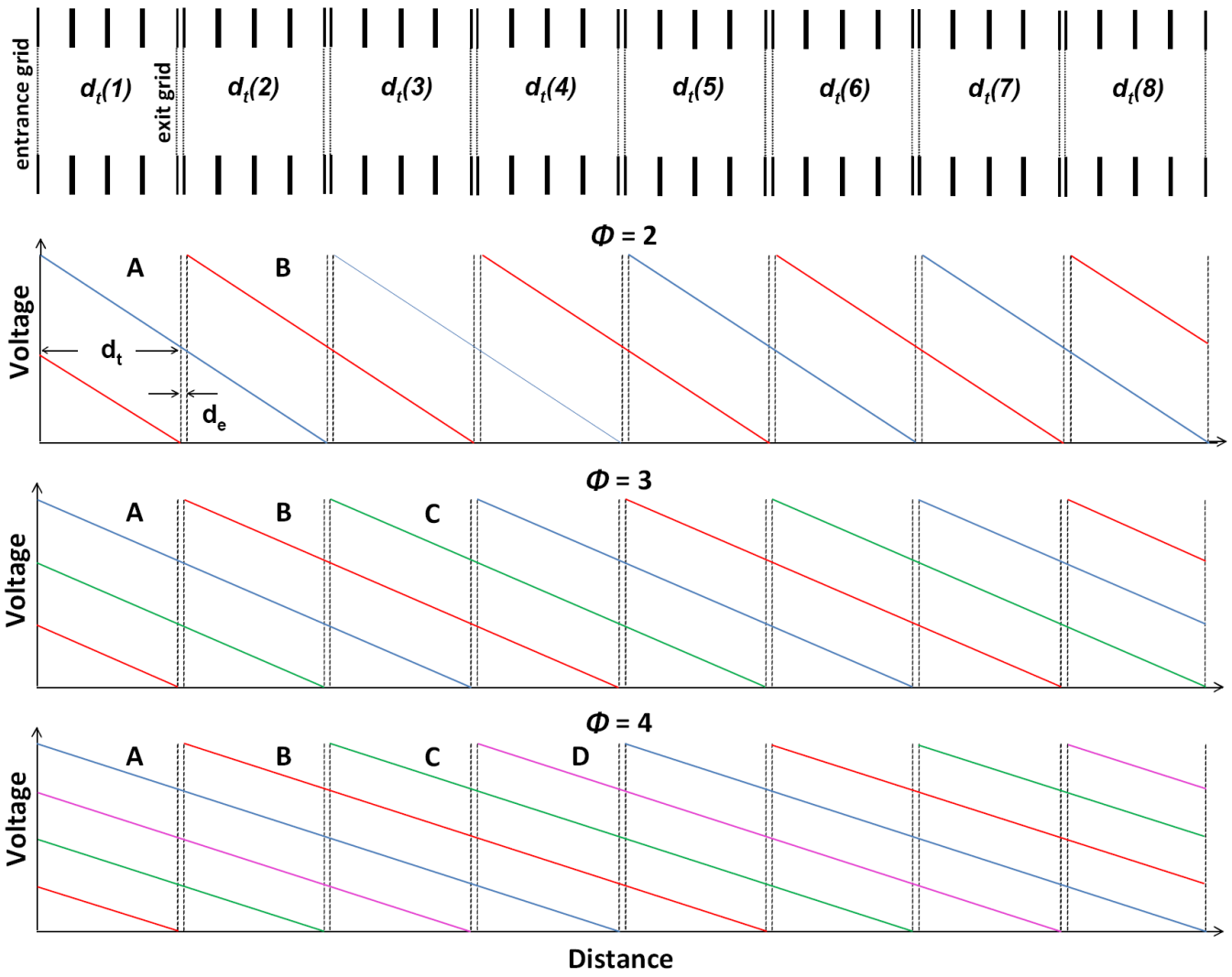

Figure 1.

Illustration of the drift regions of an OMS device. Shown are eight *d* regions (containing both d_t and d_e sections). Also shown are the field modulation settings for OMS experiments utilizing phase conditions of $\phi = 2$, 3, and 4. For the two-phase system, the blue and red traces correspond to voltage settings A and B respectively. For the three-phase system, the blue, red, and green traces correspond with the voltage settings A, B, and C respectively. Finally, for the four-phase system, the blue, red, green, and pink traces correspond with the voltage settings A, B, C, and D.

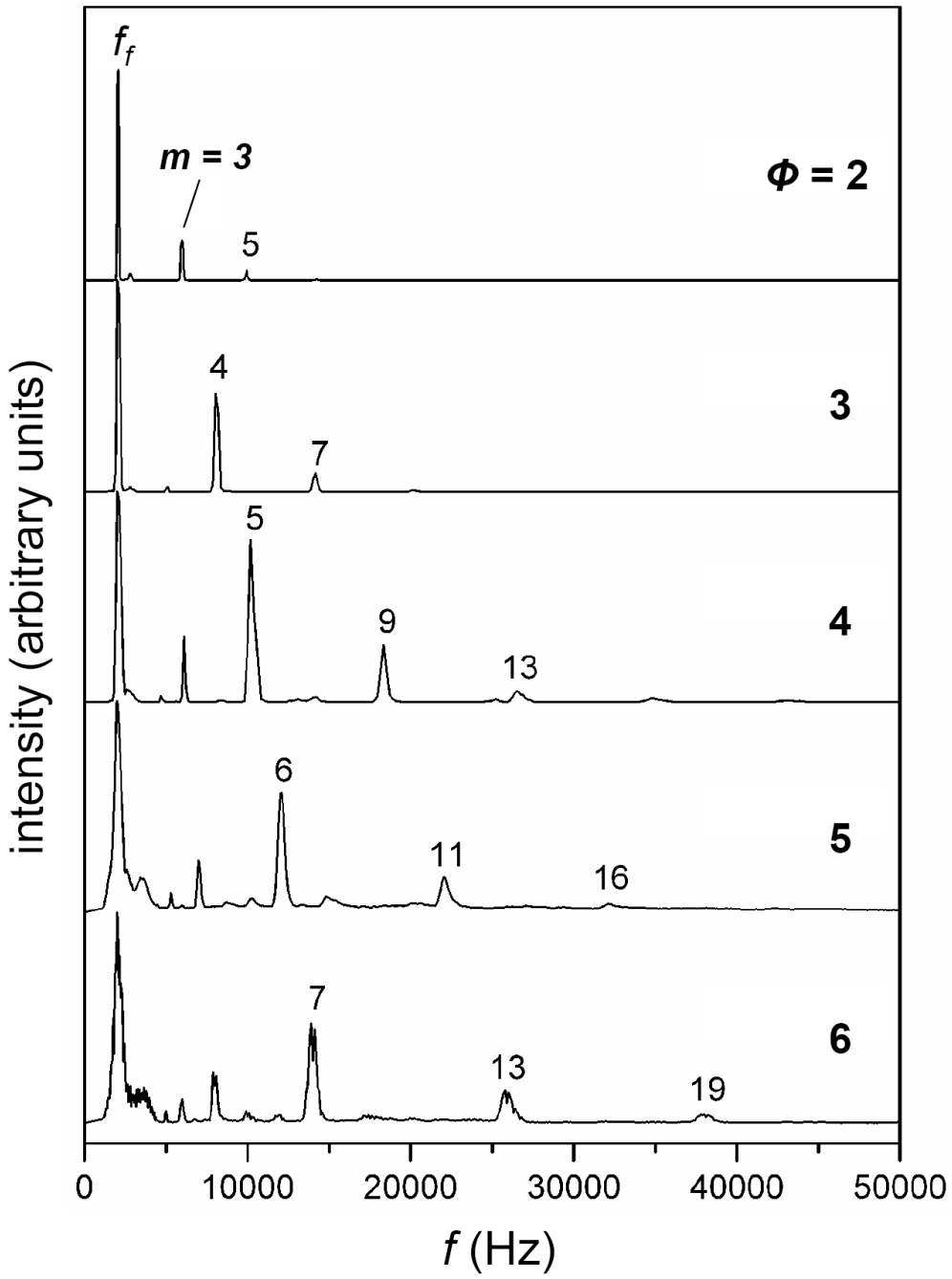

Figure 2.

Experimental OMS distributions for the $[M + Na]^+$ ion of raffinose (a three residue oligosacharride) obtained upon electrospray ionization. The data are plotted as a function of ϕ with the plots (top to bottom) representing a range of $\phi = 2$ to 6. Also depicted are the *m* values for specific overtone frequencies that permit ion transmission.

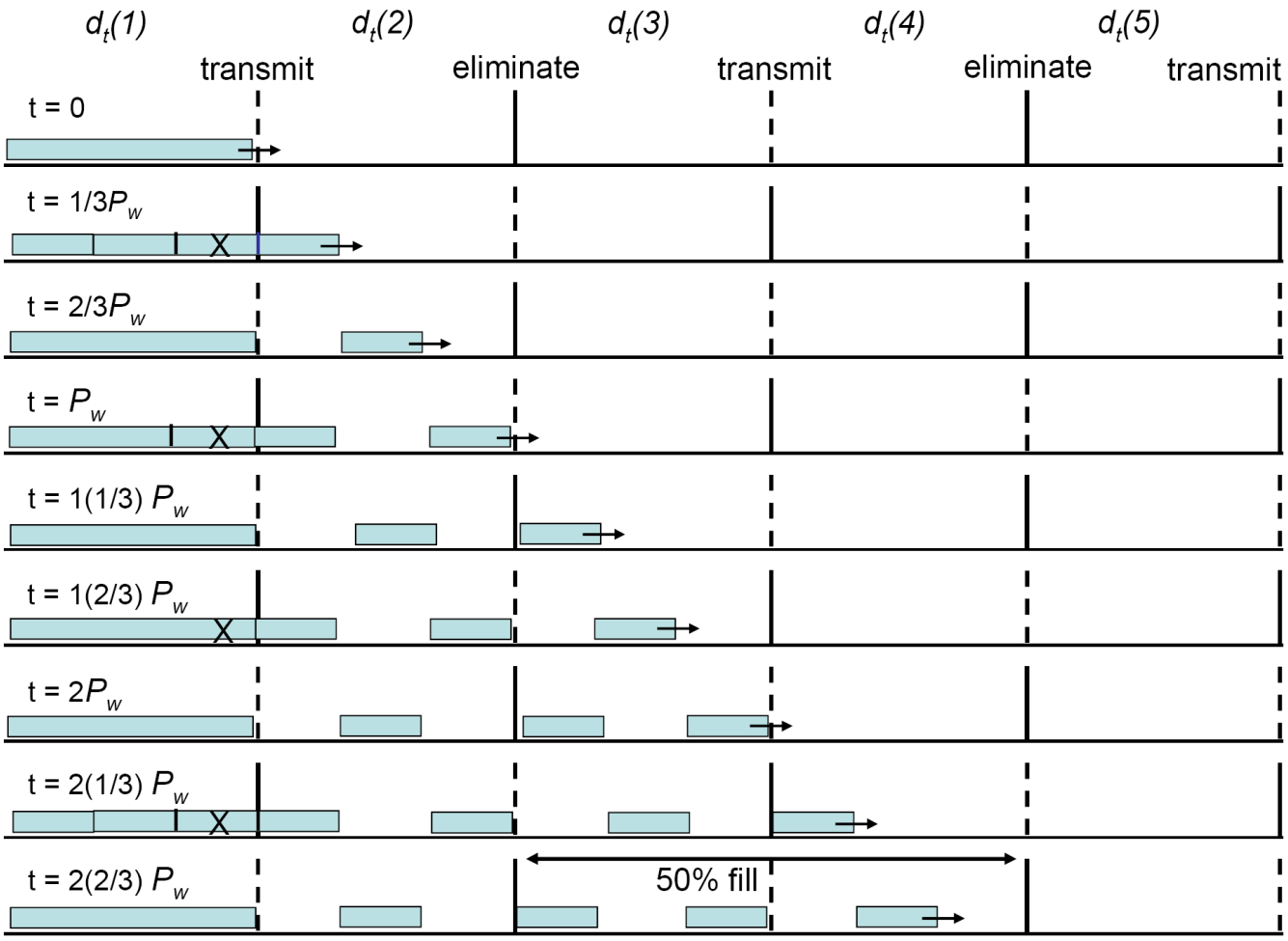

Figure 3.

Illustration of the effect of overtone frequency on ion transmission. A continuous ion beam filling the $d_t(1)$ region followed by transmission of portions of the ion beam is shown. d_t regions are indicated above each successive region and d_e regions are denoted as either elimination or transmission. Also shown is the field application time (t) as a function of the f_f time (T). d_e regions alternate between elimination (gates) and transmission (grids) conditions. This illustration shows a two-phase system where two field settings are required to complete a transmission/elimination cycle. The m = 3 harmonic frequency (2nd overtone) is represented here.

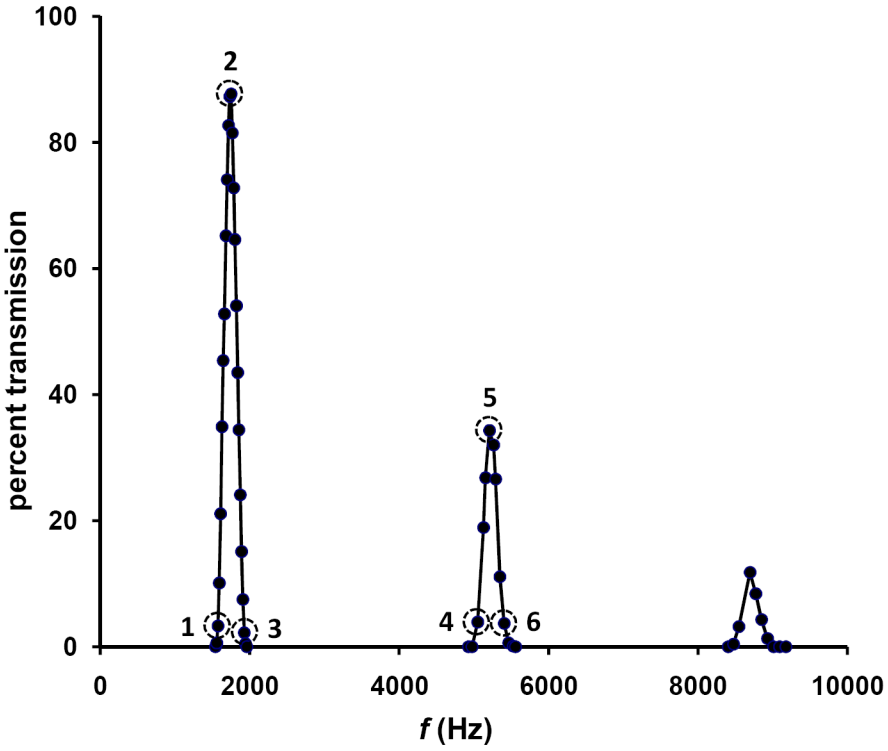

Figure 4.

OMS peak profiles obtained from ion trajectory simulations. Simulations have been performed for an OMS approach utilizing $\phi = 2$ and $n = 11$. Peaks have been modeled for the fundamental frequency as well as the $m = 3$ and $m = 5$ harmonic frequencies (2^{nd} and 4^{th} overtones). Dashed-line circles are used to indicate the ion transmission profiles (Figures 5 and 6) of ions in the $d_t(1)$ region (Figures 1 and 3) for the given frequency (see text for details).

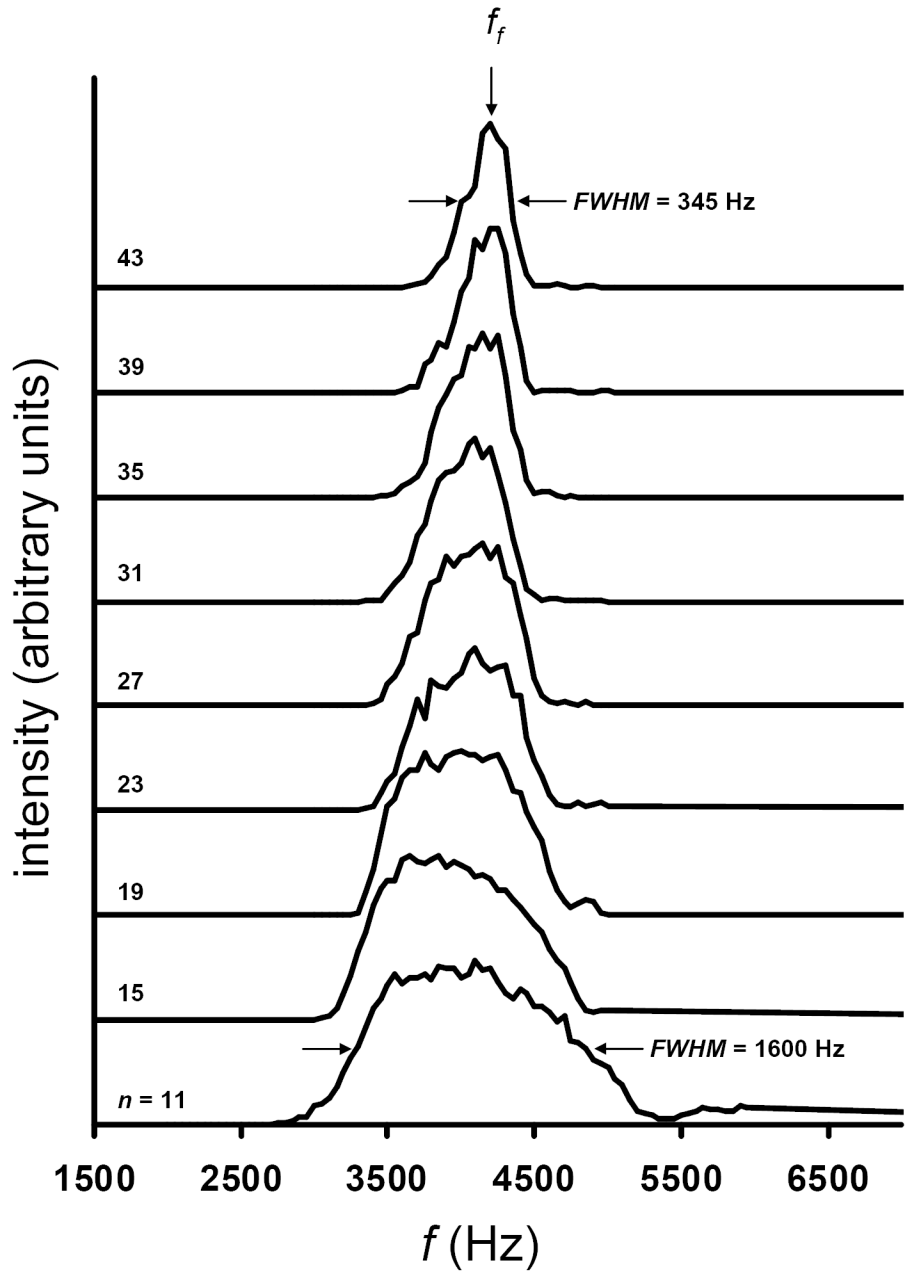

Figure 5.

Experimental OMS distributions for the $[M + Na]^+$ ion for the trisaccharide melezitose. The plots show a progression of OMS distributions as a function of *n*. The data span the range of that collected using $n = 11$ *d* regions (bottom trace) to $n = 43$ *d* regions (top trace). The position of f_f is shown with an arrow. Additionally, the peak widths (FWHM) for the OMS distributions for $n = 11$ and $n = 43$ are noted. Here OMS conditions of $\phi = 4$ and $m = 1$ are utilized. Other experimental conditions include $E = 10\ V \cdot cm^{-1}$ and $T = 300$ K. l_t and l_e region lengths of 2.83 cm and 0.24 cm, respectively have been used in the experiment.

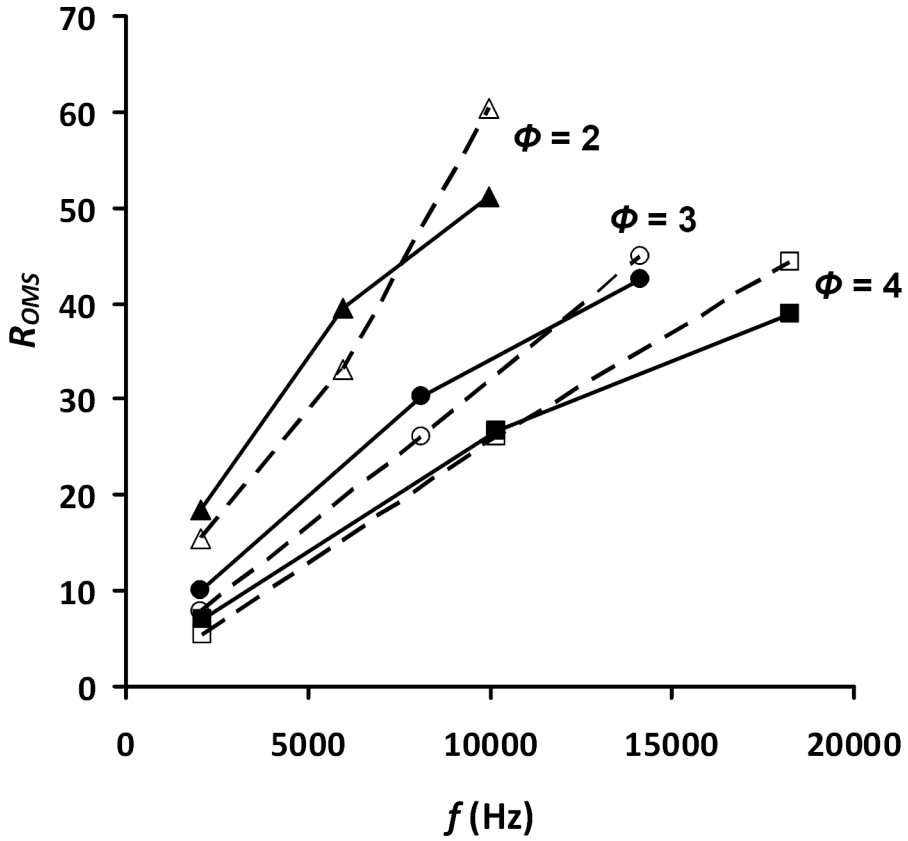

Figure 6.

Plot of calculated and experimental R_{OMS} dependence on the applied frequency for OMS approaches using $\phi = 2$ (triangles), $\phi = 3$ (circles), and $\phi = 4$ (squares). Solid symbols represent R_{OMS} obtained from Equation 20; open symbols represent experimental results for the respective values of ϕ. Only values for $h = 1$ to 3 are shown for each value of ϕ. Conditions for the experiment and the calculation include $E = 10$ V·cm^{-1} and $T = 300$ K. Additionally, the values for l_t and l_e (5.6 cm and 0.24 cm, respectively, in Figures 2, 4, and 5) have been used for the calculation. A value of 22 has been used for n for all phases.

Table 1

Definitions for variables and descriptive terms.

Variable	Definition
D	diffusion coefficient
k_b	Boltzmann's constant
T	Temperature
K	ion mobility
E	elementary charge
t_d	Measured drift time
Δt	width at half maximum of intensity peak (in time)
E	drift field
L	drift region total length
ΔL	width at half maximum of intensity peak (in length)
R_{IMS}	resolving power for IMS
R_{OMS}	resolving power for OMS
d	OMS drift region segment
d_t	ion transmission region of d
l_t	length of the ion transmission region of d
d_e	ion elimination region of d
l_e	ion elimination region of d
n	number of d regions in OMS separation device (positive integers)
ϕ	OMS system phase (positive integers)
m	harmonic frequency number (determined by ϕ and h)
j	index for field array regions in ion trajectory simulations (zero and positive integers)
h	index to relate OMS phase and harmonic frequency (positive integers)
$\sqrt{\overline{r^2}}$	root mean square ion displacement due to mobility
θ	randomization angle for ion trajectory simulations
P_{w1}	pulse width corresponding with the OMS peak apex frequency setting
P_{w2}	pulse width corresponding with the base of the OMS peak frequency setting
f_f	fundamental frequency determined from the time required for an ion to travers a single d region
f_m	harmonic field application frequency setting
f_1	frequency setting corrresponding with the apex of the OMS peak
f_2	frequency setting corresponding with the base of the OMS peak
Δf_{FWHM}	full width at half maximum peak height of the OMS peak
v_{dif}	velocity due to ion diffusion, in this case directed against mobility
σ	standard deviation of the OMS peak using the peak apex as the mean
C_1	a constant associated with converting standard deviation into FWHM of a guassian distribution
C_2	a constant associated with converting the diffusion term in the R_{OMS} equation with R_{IMS}
Ω	ion collision cross section
P	buffer gas pressure
m_I	mass of the ion

Variable	Definition
m_B	mass of the buffer gas
N	neutral number density under STP conditions

Table 2

Calculated R_{OMS} for different values for l_t and l_e.

Dimensions		R_{OMS}		
l_t (cm)	l_e (cm)	$m = 1$	$m = 3$	$m = 5$
1.4	0.24	17.0	30.0	35.4
2.8	0.24	17.7	34.6	42.7
5.6	0.24	18.5	39.5	51.1
11.2	0.24	19.2	44.4	60.0
1.4	5.6	52.6	76.9	84.7
2.5	2.5	29.2	51.7	61.2
5.6	1.4	21.8	45.4	58.1
5.6	0.12	18.2	38.8	50.3
5.6	0.24	18.5	39.5	51.1
5.6	0.48	19.2	40.7	52.6